Femtosecond laser ablation of silicon in air and vacuum

Zehua Wu (吴泽华), Nan Zhang (张 楠), Mingwei Wang (王明伟), and Xiaonong Zhu (朱晓农)***

Key Laboratory of Optical Information Science and Technology, Ministry of Education, Institute of Modern Optics, Nankai University, Tianjin 300071, China

**Corresponding author: xnzhu1@nankai.edu.cn; **corresponding author: wangmingwei@nankai.edu.cn*

Received March 18, 2011; accepted April 11, 2011; posted online July 29, 2011

Femtosecond (fs) pulse laser ablation of silicon targets in air and in vacuum is investigated using a time-resolved shadowgraphic method. The observed dynamic process of the fs laser ablation of silicon in air is significantly different from that in vacuum. Similar to the ablation of metallic targets, while the shock wave front and a series of nearly concentric and semicircular stripes, as well as the contact front, are clearly identifiable in the process of ablation under 1×10^5 Pa, these phenomena are no longer observed when the ablation takes place in vacuum. Although the ambient air around the target strongly affects the evolution of the ablation plume, the three rounds of material ejection clearly observed in the shadowgraphs of fs laser ablation in standard air can also be distinguished in the process of ablation in vacuum. It is proven that the three rounds of material ejection are caused by different ablation mechanisms.

OCIS codes: 320.7120, 140.7090, 320.7130.
doi: 10.3788/COL201109.093201.

Femtosecond (fs) laser ablation has been encountered and increasingly studied in many scientific and industrial areas since the last decade. In particular, applications of fs laser ablation in micro-machining[1−6], generation of nanoparticles[7], formation of nanostructures[8], and deposition of thin films[9] have advanced rapidly, being accompanied by many in-depth investigations of the subject of light-matter interaction. Among these developments, a number of powerful diagnostic techniques have been employed, such as plume self-emission probing[10,11], time of flight mass spectroscopy[12], soft X-ray absorption spectroscopy[13], time-resolved shadowgraphy[14,15], time-resolved reflectivity[16,17], and fs electron pulse probing[18]. The theoretical simulations of molecular dynamics[19,20] are also adopted to investigate the dynamic process of fs laser ablation. Various physical models, such as coulomb explosion[21], phase explosion[22], critical point phase separation[23], fragmentation[24], and thermoelastic wave mechanism[25], are proposed to describe the possible photomechanical and photothermal mechanisms involved in fs laser ablation. Nevertheless, further research is still required toward a complete understanding of the fundamental mechanisms for fs laser ablation.

The time-resolved shadowgraphic method can provide us with useful evolutionary information of fs laser ablation by giving an intuitional display of its dynamic process. A detailed comparison of the dynamic processes of fs laser ablation of solid targets in air and in vacuum is very helpful in unveiling the underlying mechanisms of fs laser ablation. In this letter, a side-by-side comparison of the time-resolved shadowgraphs of fs laser ablation of silicon targets under 1×10^5 and 1×10^{-3} Pa is presented. These shadowgraphs are experimentally recorded for various observation time windows with a maximum time delay of up to 8.3 ns. Through such a comparison, it can be found that the ambient air around the target affects the dynamic process of fs laser ablation significantly. It also helps in recognizing that the ejection or expansion of the ejected material undergoes three distinctive stages characterized by different expansion dynamics and different mechanisms during the time period of the initial 8.3 ns.

A schematic diagram of our experimental setup is shown in Fig. 1. It represents a typical optical arrangement for the pump-probe technique in recording the time-resolved shadowgraphs of fs laser ablation of silicon under either 1×10^5 or 1×10^{-3} Pa. The 50-fs near infrared laser pulse output from a Ti:sapphire fs laser amplifier system (HP-Spitfire, Spectra-Physics, Inc., USA) is divided by the beam splitter into a pump or excitation pulse and a probe pulse with an energy ratio of 70:30. The pump pulse with a central wavelength near 800 nm is focused on the target surface by a 10× objective lens (NA = 0.25) after being reflected by four 45° steering mirrors and passing through the flange optical window of the vacuum chamber. The probe pulse is frequency doubled by a 2-mm-thick β-BaB_2O_4(BBO) crystal with type I phase matching, and the 400-nm blue-color probe pulse illuminates the ablation region along a direction perpendicular to the pump beam. Another 4× objective lens is used to collect the probe beam and to form the shadowgraphic image of the material ejection induced by the ablation at the sensor plane of a monochromatic charge coupled device (CCD) camera (LU135M, Lumenera Inc., Canada). A 400-nm band pass filter and a few neutral density filters are used to prevent the residual 800-nm pump light within the probe beam and the fluorescence induced by the ablation from entering the CCD camera.

Each time after a pump laser pulse strikes the target and a shadowgraphic picture is taken, the silicon target polished with sandpapers is moved to a fresh spot along the direction perpendicular to the pump beam. When the ablation takes place in air, the silicon target is deliberately placed slightly before the geometrical focus of the focal lens in order to avoid air ionization. For the purpose of having the same focal spot size at the target surface so that a meaningful comparison can be made, the target is kept at the same off-focus position when the ablations are made in vacuum.

Figure 2 shows the time-resolved shadowgraphs of 50-fs

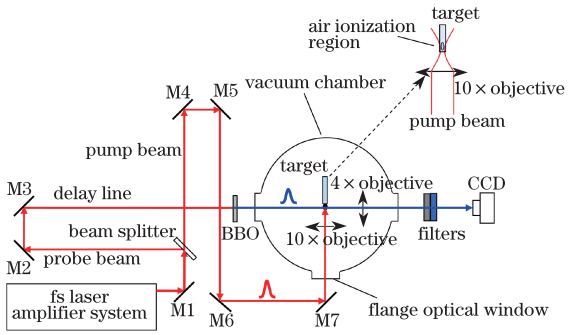

Fig. 1. Schematic diagram of the experimental setup. M1-M7: steering mirrors.

laser pulse ablation of a silicon target under 1×10^5 Pa (top row) and 1×10^{-3} Pa (bottom row), respectively. In each shadowgraph, the black part on the right represents a side view of the silicon target whereas the pump laser pulse always propagates from the left to the right as shown by the horizontal arrow in Fig. 2(a). The energy of the pulse that impinges on the target surface is 0.14 mJ, which leads to a pulse energy fluence of $\sim$32 J/cm^2 at the surface of the silicon target.

From the shadowgraphs shown in the top row of Fig. 2, the following four distinctive features may be readily identified. First, a bulge protrudes from the target surface 50-ps after the laser pulse strikes it (see Fig. 2(a)), namely at 50-ps delay time, the first round material ejection has occurred, which contributes to the formation of the shock wave front occurring later. The narrow track present in front of the target is the result of the absorption of the probe light by the air plasma, produced by the reflected fs laser pulse (note that because the target is placed before the actual focusing point, this leads to the reflected beam being focused just in front of the target). This is further verified by the fact that as the target is tilted, the narrow plasma track also tilts away from the direction of the incident light and points to the same direction as that of the reflection. Second, a hemispherical shock wave emerges, and a series of nearly concentric and semicircular stripes are observed within the shock wave front at around 1-ns delay time. These nearly concentric and semicircular stripes are about to disappear for a delay time of 3 ns. Third, a distinctive protuberance structure sticks out from the hemispherical shock wave front, and the contact front is observed inside the ablation plume, which is generated due to the second round material ejection (see Fig. 2(e)). The radius of the shock wave front, as well as the distance from the contact front to the target surface, increases with increasing delay time. Fourth, dense ablated material noticeably emerges near the target surface at 5.5-ns delay time (see Fig. 2(i)). From the shadowgraphs in Figs. 2(i), (k), and (m), it can be seen that such dense ablated material associated with the third round material ejection expands with dynamics different from the ejected material forming the contact front.

For the shadowgraphs recorded under 1×10^{-3} Pa and reproduced in the bottom row of Fig. 2, four distinctive characteristics can also be found. First, a bulge similar to that recorded under 1×10^5 Pa appears at 50-ps delay time (see Fig. 2(b)), but the narrow track of air plasma, as that shown in Fig. 2(a), is no longer present because of the state of sufficiently high vacuum. Second, the shock wave front and the nearly concentric and semicircular stripes recorded in the process of ablation under 1×10^5 Pa are also not observed in the whole plume evolution process. The ejected target material has no clear borderline, except that several stripes parallel to the target surface within the ejected material region can be seen at 1-ns delay time (see Fig. 2(d)). Third, unlike the situation of laser ablation under 1×10^5 Pa for delay time of 3 and 5 ns, the contact front is also not seen. Fourth, for 5.5-ns delay time, similar to the corresponding case under 1×10^5 Pa, a dark bulge associated with a new round of target material ejection can be clearly observed near the target surface. Such a new ejection is likely to be composed of larger or denser particles as it appears much darker in the shadowgraphs. The ejected material of this round further expands from 5.5 to 8.3 ns delay time. Because of the state of vacuum, such an expansion is noticeably faster than that in normal air.

By comparing and analyzing the distinctive features of the time-resolved shadowgraphs of the fs laser ablation of silicon under 1×10^5 and 1×10^{-3} Pa, some important insights into the ultrafast ablation process of interest can be obtained. As mentioned earlier, the laser fluence on the target surface in our experiments is $\sim$32 J/cm^2. According to theoretical calculations[19,23], such high laser fluence can lead to the atomization of the target material and form dense plasma of high temperature and

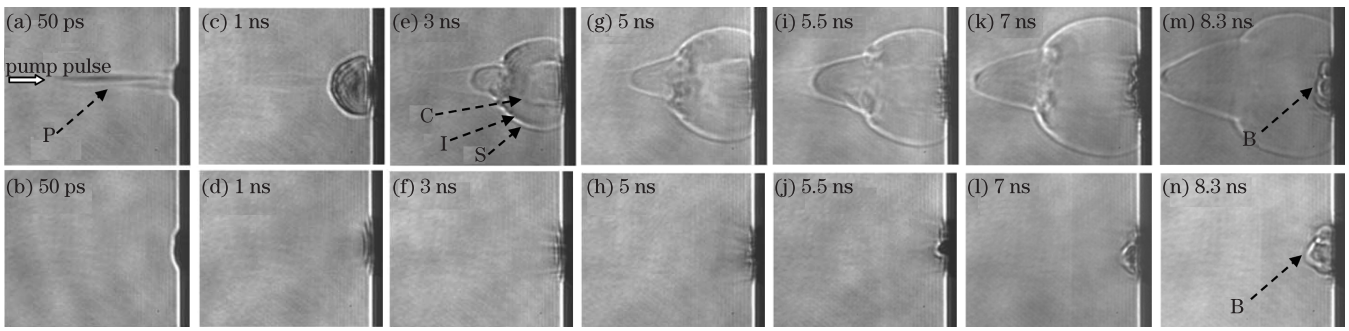

Fig. 2. Shadowgraphs of fs laser ablation recorded at the indicated delay time after a 50-fs laser pulse of 0.14-mJ strikes the silicon target under 1×10^5 Pa (top row) and 1×10^{-3} Pa (bottom row), respectively. For each shadowgraph, the laser pulse comes from the left, and the black part is a side view of the silicon target. (a): a track of air plasma formed by the reflected laser is indicated by P. (e): S, I, and C respectively represent the shock wave front, the ionization front, and the contact front. In Figs. (m) and (n): B represents the boundary formed by the third round material ejection; Each frame size is 170×145 (μm).

pressure. The dark bulge that appeared in Figs. 2(a) and (b) is thus composed of high-density plasma generated in the atomization process of the ablated target. The ions and atoms in the plasma will quickly expand and compress the ambient air to form the shock wave front, which corresponds to the first round material ejection. The phenomenon of the expansion of the ablated material recorded by the shadowgraph of 50-ps delay time under both 1×10^5 and 1×10^{-3} Pa that looks relatively similar indicates that the atomization of the target for the initial 50-ps delay time occurs both in air and in vacuum.

The fact that the nearly concentric and semicircular stripes existing within the shock wave front for a specific time period under 1×10^5 Pa not being present in the case of the ablation under 1×10^{-3} Pa proves that ambient air is critical for the formation of the stripe pattern. Regular stripes are observed only around 1-ns delay time and disappear with the elapse of time, which is also true in the process of fs laser ablation of aluminum[14,26]. We, thus, tend to believe that the formation of the stripes is independent of any specific target material, and most probably, it is a rather generic phenomenon for material ablation of ultrafast laser ablation. During the evolution of the shock wave, the ejected ablation material undergoes a special transient state associated with a unique refractive index field, which leads to the diffraction of the probe light to form the stripes.

The contact front observed at 3-ns delay time under 1×10^5 Pa is also not observed under 1×10^{-3} Pa (see Figs. 2(e) and (f)). This implies that the stagnation of the ambient air to the ejected target material plays an important role in the formation of the contact front[27]. The speed of material particles induced by the laser ablation can be effectively reduced during the collision with ambient air, which also leads to the spatial accumulation or piling up of the ejected particles from the target, and thus results in the formation of the contact front. The stagnation effect of the ambient air will be negligible for the ablation under 1×10^{-3} Pa. In this case, the particles ejected from the target move freely and do not accumulate spatially, thus the contact front is not observed, as shown in Fig. 2(f).

When the air is present, as can be seen from Figs. 2(i), (k), and (m), the lateral extension of the ablated area on the target surface appears larger than the corresponding cases in Figs. 2(j), (l), and (n), respectively. The boundary of the third round ejected material is also more prominent at the center for the case of ablation in vacuum than in air, which is a result of the less uniform distribution of heating and stress across the laser ablation site. Therefore, this further demonstrates that the ambient air also plays an important role in assisting heat dissipation across the target surface.

The protuberance at the middle of the hemispherical shock wave front, as shown in Figs. 2(e) and (g), manifests the interesting interaction between the hemispherical shock wave caused by ablation and the cylindrical shock wave induced by the expansion of the narrow track of air plasma. The latter is related with air ionization and is clearly evident in Fig. 2(a) for 50-ps delay time. As the cylindrical shock wave expands with time elapsing, the air density in its interior must be significantly reduced, and thus a low pressure zone is formed. The hemispherical shock wave front is thus disrupted by this expanding cylindrical shock wave front. In particular, the air molecules at the interface between the hemispherical shock wave front and the cylindrical shock wave front may gain greater forward acceleration than the molecules at the other part of the semicircular shock wave front because of the sucking force caused by the pressure difference between the two regions. It is such an accelerated portion moving faster than the other part that forms the protuberance sticking out from the hemispherical shock wave front.

With the shadowgraphs shown in the top row of Fig. 2, the respective propagation speed of the second round ejected material and the third round ejected material in the case of 1×10^5 Pa can be readily derived. The estimated propagation speed of the ejected material of the second round eruption for the first 3 ns is ~12.6 km/s, which contrasts the speed of ~5.9 km/s for the third round ejected material front (marked by letter B in Fig. 2(m)) that is also estimated for the first 3 ns since its start. Meanwhile, the propagation speed of the shock wave front induced by the first round material ejection is ~21 km/s in the first 3 ns. Therefore, it is very clear that different expansion dynamics exist for the three rounds of material ejection caused by femtosecond laser ablation. Interestingly, for laser ablation that takes place under 1×10^{-3} Pa, the propagation speed of the ejected material of the third round is approximately 8.8 km/s during the first 3-ns time interval since its start. Therefore, the stagnation of the ambient air of 1×10^5 Pa leads to a decrease in the propagation speed of the ejected material of the third round by ~33%.

As mentioned above, the formation of the contact front is largely due to the stagnation of the residual ambient air inside the shock wave profile, as shown in Figs. 2(e) and (g). Without the effective stagnation of the residual ambient air within the shock wave, the clear boundary in the front of the ejected material cannot be formed. This is evident in the corresponding shadowgraphs obtained under 1×10^{-3} Pa, which are given in Figs. 2(f) and (h), where no contact front exists. However, for the shadowgraph taken at 8.3-ns delay time, clear boundary of the ejected material (also marked by letter B) may be seen in Fig. 2(n), even though it is under the vacuum state of 1×10^{-3} Pa. This is because the material ablation during the initial 5-ns generates some gaseous material around the target surface, and this initially ablated gaseous material may act like that of the ambient air toward the later material ejection. This means that it is the stagnation of this initial ablation-induced plume gases to the third round ejected material that leads to the formation of the clear boundary observed at 8.3 ns under 1×10^{-3} Pa. This further illustrates the intermittent material ejection nature under the femtosecond laser ablation.

When a focused high-fluence fs laser pulse strikes the target, the target material in the upper surface layers will be ablated off through the atomization process and decompose into the atomic species (neutrals and ions)[10,13,19], which leads to the first round material ejection and forms the shock wave front. The laser-irradiated region will become extremely heated, leading to a state of ultrahigh pressure[14,22,28]. In such a case, the sec-

ond round material ejection occurs due to the possible mechanisms of the mechanical fragmentation or phase explosion. The extremely high pressure within the laser-heated region releases in both forward and backward directions. The backward or the outward pressure release is accompanied by the second round material ejection, whereas the forward or inward pressure is related to a strong compression of the atoms in the interior of the target, which makes the atoms move inward and may even break the bonds of some atoms. Eventually, the atoms moving inward will stop and move backwards because of the repelling force of the interior atoms. This is how the third round material ejection is formed, which is the relaxation of inward pressure induced by the fs laser heating.

Furthermore, theoretical simulations have revealed that the material ejection due to mechanical fragmentation and phase explosion takes place within the first 5 ns right after the fs laser pulse strikes the target[22,29]. This indicates that in our case, the ejected material forming the contact front in the second round ejection should be mostly composed of nanoparticles generated through mechanical fragmentation or phase explosion. However, the mechanism for material ejection in the third round is likely to be different from the second round, thus we expect the size of the particles of the ejected material in the third round ejection to be noticeably larger than that in the second round ejection. The presence of multiple stress waves in the process of fs laser ablation has also been discussed previously[14] in analogy to a piece of stone being dropped into water. Furthermore, in our experiments, the aforementioned atomization of the target, which leads to the formation of the shock wave, is also in agreement with the results in Refs. [10,13].

In conclusion, time-resolved shadowgraphic measurements indicate that significant differences exist between the fs laser ablation of silicon targets under 1×10^5 Pa and 1×10^{-3} Pa. The ambient air around the target, acting as both a stagnation force and an effective heating dissipation factor, may greatly affect the dynamic process of fs laser ablation. The shock wave front, the nearly concentric semicircular stripes, and the contact front clearly observable in the process of fs laser ablation under 1×10^5 Pa are no longer observed under 1×10^{-3} Pa. It is further confirmed that the nearly concentric semicircular stripes in the shadowgraph of the ablation under 1×10^5 Pa for a specific delay time are independent of the type of target material. It is believed that the three rounds of consecutive material ejection exist for the fs laser ablation under either 1×10^5 or 1×10^{-3} Pa. While the first round material ejection is generated by the direct atomization of the target, the second round material ejection is most likely due to the mechanisms of mechanical fragmentation or phase explosion, and the third round material ejection should result from the tremendous repelling force associated with the extremely high pressure induced in the process of fs laser ablation.

This work was supported by the National Natural Science Foundation of China (Nos. 60637020 and 11004111), the Tianjin Natural Science Foundation (No. 10JCZDGX35100), and the Open Fund of the State Key Laboratory of Explosion Science and Technology (No. KFJJ-8).

References

1. B. N. Chichkov, C. Momma, S. Nolte, F. von Alvensleben, and A. Tünnermann, Appl. Phys. A **63,** 109 (1996).
2. Y. Wu, C. Wang, W. Jia, X. Ni, M. Hu, and L. Chai, Chin. Opt. Lett. **6,** 51 (2008).
3. Y. Li, H. Jiang, H. Yang, and Q. Gong, Chin. Opt. Lett. **3,** (suppl.) 200 (2008).
4. Y. Zhu, H. Mei, T. Zhu, J. Zhang, and S. Yin, Chin. Opt. Lett. **7**, 675 (2009).
5. W. Jia, B. Zhou, X. Li, L. Chai, R. Zhang, and C. Wang, Chin. Opt. Lett. **8**, 38 (2010).
6. Y. Zhang, X. Jia, P. Xiong, and T. Jia, Chin. Opt. Lett. **8**, 1203 (2010).
7. E. Stratakis, M. Barberoglou, C. Fotakis, G. Viau, C. Garcia, and G. A. Shafeev, Opt. Express **17**, 12650 (2009).
8. A. S. Mahmood, M. Sivakumar, K. Venkatakrishnan, and B. Tan, Appl. Phys. Lett. **95,** 034107 (2009).
9. J. Perrière, E. Millon, W. Seiler, C. Boulmer-Leborgne, V. Craciun, O. Albert, J. C. Loulergue, and J. Etchepare, J. Appl. Phys. **91,** 690 (2002).
10. S. Amoruso, R. Bruzzese, N. Spinelli, R. Velotta, M. Vitiello, X. Wang, G. Ausanio, V. Iannotti, and L. Lanotte, Appl. Phys. Lett. **84,** 4502 (2004).
11. S. Amoruso, R. Bruzzese, X. Wang, and J. Xia, Appl. Phys. Lett. **92,** 041503 (2008).
12. M. Lenner, A. Kaplan, Ch. Huchon, and R. E. Palmer, Phys. Rev. B **79,** 184105 (2009).
13. K. Oguri, Y. Okano, T. Nishikawa, and H. Nakano, Phys. Rev. B **79,** 144106 (2009).
14. N. Zhang, X. Zhu, J. Yang, X. Wang, and M. Wang, Phys. Rev. Lett. **99,** 167602 (2007).
15. X. Mao, S. S. Mao, and R. E. Russo, Appl. Phys. Lett. **82,** 697 (2003).
16. X. Wang, T. Jia, X. Li, C. Li, D. Feng, H. Sun, S. Xu, and Z. Xu, Chin. Opt. Lett. **3,** 615 (2005).
17. T. Wu, C. Zhou, E. Dai, and J. Xie, Chin. Opt. Lett. **7,** 653 (2009).
18. C. T. Hebeisen, G. Sciaini, M. Harb, R. Ernstorfer, S. G. Kruglik, and R. J. D. Miller, Phys. Rev. B **78,** 081403 (R) (2008).
19. D. Perez and L. J. Lewis, Phys. Rev. B **67,** 184102 (2003).
20. X. Liu and Y. Wang, Chin. Opt. Lett. **3,** 57 (2005).
21. W. G. Roeterdink, L. B. F. Juurlink, O. P. H. Vaughan, J. Dura Diez, M. Bonn, and A. W. Kleyn, Appl. Phys. Lett. **82,** 4190 (2003).
22. P. Lorazo, L. J. Lewis, and M. Meunier, Phys. Rev. Lett. **91,** 225502 (2003).
23. F. Vidal, T. W. Johnston, S. Laville, O. Barthélemy, M. Chaker, B. Le Drogoff, J. Margot, and M. Sabsabi, Phys. Rev. Lett. **86,** 2573 (2001).
24. D. Perez and L. J. Lewis, Phys. Rev. Lett. **89,** 255504 (2002).
25. X. Wang and X. Xu, J. Thermal Stresses, **25,** 457 (2002).
26. Z. Wu, X. Zhu, and N. Zhang, J. Appl. Phys. **109,** 053113 (2011).
27. G. Callies, P. Berger, and H. Hugel, J. Phys. D **28,** 794 (1995).
28. E. G. Gamaly, S. Juodkazis, K. Nishimura, H. Misawa, B. L. Davies, L. Hallo, P. Nicolai, and V. T. Tikhonchuk, Phys. Rev. B **73,** 214101 (2006).
29. C. Cheng and X. Xu, Phys. Rev. B **67,** 165415 (2005).